Unified thermo-compositional-mechanical framework for reservoir simulation

Garipov, T. T.; Tomin, P.; Rin, R.; Voskov, D. V.; Tchelepi, H. A.

DOI
10.1007/s10596-018-9737-5

Publication date
2018

Document Version
Final published version

Published in
Computational Geosciences

Citation (APA)
Garipov, T. T., Tomin, P., Rin, R., Voskov, D. V., & Tchelepi, H. A. (2018). Unified thermo-compositional-mechanical framework for reservoir simulation. *Computational Geosciences*, *22*(4), 1039-1057. https://doi.org/10.1007/s10596-018-9737-5

Computational Geosciences (2018) 22:1039–1057
https://doi.org/10.1007/s10596-018-9737-5

ORIGINAL PAPER

Unified thermo-compositional-mechanical framework for reservoir simulation

T. T. Garipov[1] · P. Tomin[1] · R. Rin[1] · D. V. Voskov[2] · H. A. Tchelepi[1]

Received: 10 April 2017 / Accepted: 7 March 2018 / Published online: 11 April 2018

Abstract

We present a reservoir simulation framework for coupled thermal-compositional-mechanics processes. We use finite-volume methods to discretize the mass and energy conservation equations and finite-element methods for the mechanics problem. We use the first-order backward Euler for time. We solve the resulting set of nonlinear algebraic equations using fully implicit (FI) and sequential-implicit (SI) solution schemes. The FI approach is attractive for general-purpose simulation due to its unconditional stability. However, the FI method requires the development of a complex thermo-compositional-mechanics framework for the nonlinear problems of interest, and that includes the construction of the full Jacobian matrix for the coupled multi-physics discrete system of equations. On the other hand, SI-based solution schemes allow for relatively fast development because different simulation modules can be coupled more easily. The challenge with SI schemes is that the nonlinear convergence rate depends strongly on the coupling strength across the physical mechanisms and on the details of the sequential updating strategy across the different physics modules. The flexible automatic differentiation-based framework described here allows for detailed assessment of the robustness and computational efficiency of different coupling schemes for a wide range of multi-physics subsurface problems.

Keywords Geomechanics · Thermal-compositional-mechanics · Reservoir simulation · Multiphase flow · Multi-physics coupling

1 Introduction

The simulation of complex subsurface processes entails solving the governing equations that describe multiphase flow, multi-component transport, thermal effects, and geomechanics. Enhanced oil recovery (EOR) processes, such as the near-miscible gas injection and thermal recovery methods, are a primary target for reservoir simulation. Such EOR processes are characterized by complex multi-component interactions that lead to multiple phase changes when coupled with the flow. The evolution of the pressure, saturations, and temperature can be highly nonlinear and quite complex for large-scale reservoirs. Changes in the pressure, temperature, and saturations can induce complex interactions with the solid structure and lead to changes in the stress and strain fields within the reservoir and its surrounding formations. The nonlinear interactions among different physical mechanisms impose very strict requirements on the discretization and solution schemes. Detailed assessment of the truncation errors and the numerical stability of the discrete scheme are critically important. In order for the simulation framework to be useful, it is important to ensure robust and efficient performance, and this depends very strongly on the nonlinear convergence behavior and the computational efficiency of the solution strategy across the parameter space of practical interest.

The fully implicit (FI) approach is attractive for general-purpose simulation due to its unconditional stability. The FI

✉ T. T. Garipov
tgaripov@stanford.edu

✉ P. Tomin
ptomin@stanford.edu

✉ H. A. Tchelepi
tchelepi@stanford.edu

R. Rin
iskhakov@stanford.edu

D. V. Voskov
D.V.Voskov@tudelft.nl

[1] Energy Resources Engineering, Stanford University, Stanford, CA 94305, USA

[2] Delft University of Technology, 2600 GA, Delft, The Netherlands

scheme is also referred to as the "simultaneous solution" or monolithic strategy. However, FI approaches are computationally expensive and require the development of a unified flow–energy–geomechanics simulation framework [23, 66]. In addition, the domain for the mechanics problem is usually significantly larger than the target reservoir (oil, gas, water). Consequently, fully coupled solutions that include the full mechanics problem can become quite expensive. Another disadvantage of the FI approach is that the resulting linear systems are nonsymmetric with mixed character (e.g., elliptic, parabolic, hyperbolic); dealing with such linear systems in a robust and efficient manner requires the development of sophisticated multi-stage preconditioning techniques [8, 71].

The development and application of sequential-implicit (SI) methods are motivated by the desire to avoid developing a framework for fully coupled multi-physics problems and the associated requirement of specialized multi-stage linear solvers. In the computational geoscience community, different types of sequential coupling between the flow and mechanics problems are used. Iterative coupling schemes can be explicit, loosely coupled, or sequential implicit [15]. In iterative coupling, the system of governing equations is divided into several physics sub-problems, each of which can be solved by a different method, including dedicated nonlinear and linear solvers. For example, a general class of multigrid methods [18, 57] is known to be effective for the flow and mechanical parts, whereas a simple factorization strategy (e.g., incomplete LU factorization) is quite efficient for the transport problem [62].

The coupled flow and geomechanics problem was implemented in an explicitly coupled fashion [47, 72], where each physical process was solved separately with a partial update of the solution between steps. In this approach, the convergence of the full system of the governing equations often was not checked. Although this method can be efficient and accurate in some situations, it does not guarantee the correctness of the solution. Later, a loosely coupled scheme was proposed for the solution of flow and geomechanics problems [5, 55]. This approach is similar to the explicitly coupled scheme, with an occasional resolution of the coupling between the different physical systems. In some cases, the loosely coupled scheme can produce results in reasonable agreement with the FI approach along with good computational performance [43, 54].

In the last few years, several SI schemes have been proposed and analyzed [20, 49, 55, 58, 59, 63]. SI schemes have several advantages. They allow for using separate modules for each physical process, use of advanced single-physics linear solvers (e.g., multigrid for the near-elliptic pressure), and separate discretization of the different physics in different spatial domains [38]. Moreover, for a few coupled problems, specific SI splitting strategies can yield unconditionally stable and computationally scalable solutions [3, 31, 41].

Developing fast, robust, and general-purpose simulation platforms capable of solving a wide range of problems, such as multiphase flow, energy transport, and mechanical deformation, is of strong interest and poses significant and exciting challenges. General-purpose simulators capable of solving challenging problems employ either FI or a specific SI scheme. Many research simulators employ sequentially iterative strategies (e.g., Subsurface Transport Over Multiple Phases (STOMP) [65], TOUGHT+FLAC [53], IPARS-JAS3D [42], and OpenGeoSys [33]. However, without fully implicit reference solutions, it is often unclear whether the solutions are accurate, and it is nearly impossible to ascertain where in the parameter space can these simulators be used. These concerns are addressed in fully coupled multi-physics simulators, such as DuMuX [19] and MRST [27, 37]. However, the published results are limited to relatively simple multi-physics problems and small reservoir models. None of the available multi-physics simulators is capable of running both fully implicit and sequential-implicit approaches within the same platform, and there is a clear lack of accurate and systematic studies of different coupling strategies. One available comparison [40], performed in PANDAS [17], is limited to simplified flow-mechanics physics without nonlinear effects.

In this paper, we describe a reservoir simulation framework implemented in the Automatic Differentiation General Purpose Research Simulator (AD-GPRS) [2]. We solve the system of nonlinear governing equations in fully implicit mode and in a variety of SI strategies. The framework employs the Automatically Differentiable Expression Templates Library (ADETL) to compute the Jacobian [67]; this library helps us obtain exact derivatives for complicated settings, such as when the phase equilibrium calculations [61] or the plastic nature of the deformation [21] are involved in the nonlinear evolution of the solution. All the coupling schemes are implemented in a unified manner, and the choice of the solution strategy can be easily made in the input "deck" [51, 52]. We use five test problems to demonstrate the performance of fully and sequentially implicit coupling approaches for complex processes that involve geomechanics. We show that the framework allows for modeling nonlinear multi-physics problems using different solution schemes.

2 Governing equations and mathematical models

In this section, we present the mathematical model that describes the flow and transport of mass and energy coupled

with mechanical deformation in heterogeneous geological formations. In the description, we follow a macroscale continuum representation of the physical processes, where the flow is described by Darcy's law and geomechanical interactions follow the generalized Biot's theory [12].

2.1 Mass and energy conservation equations

The governing equations describing a thermal multiphase multi-component flow in porous media contain conservation equations of mass, energy, and associated constraints. The mass conservation equations can be written as:

$$\frac{\partial}{\partial t}\left(\phi \sum_{j=1}^{n_p} x_{\mathrm{ij}} \rho_j S_j\right) + \nabla \cdot \left(\sum_{j=1}^{n_p} x_{\mathrm{ij}} \rho_j \mathbf{v}_j\right) + \sum_{j=1}^{n_p} x_{\mathrm{ij}} \rho_j q_j = 0, \quad i = 1 \ldots n_c, \tag{1}$$

where i and j indicate a component and a phase, respectively, and n_c and n_p are the total number of components and phases, respectively; ϕ is the porosity; S_j, x_{ij}, p_j, and ρ_j are the phase saturations, compositions, phase pressures, and densities, respectively; q_j is the source term. The phase velocity $\boldsymbol{v}_j$ is represented by Darcy's law:

$$\boldsymbol{v}_j = -\mathbf{k}\frac{k_{\mathrm{rj}}}{\mu_j}\left(\nabla p_j - \rho_j g\right), \tag{2}$$

where k is the absolute-permeability tensor, k_{rj} is the phase relative permeability, μ_j is the phase viscosity, and g is gravity acceleration.

We assume thermal equilibrium between the fluids and the solid skeleton; as a result, the overall energy balance can be written as:

$$\frac{\partial}{\partial t}\left(\phi \sum_{j=1}^{n_p} U_j \rho_j S_j + (1-\phi) U_r\right) + \nabla \cdot \left(\sum_{j=1}^{n_p} h_j \rho_j \boldsymbol{v}_j\right) - \nabla \cdot (\kappa \nabla T) + \sum_{j=1}^{n_p} h_j \rho_j q_j = 0, \tag{3}$$

where T is the temperature (thermal equilibrium between fluids and solid skeleton is assumed), κ is the thermal conduction coefficient, U_j and U_r are the phase and rock internal energies, respectively, and h_j is the phase enthalpy. Here we define $U_j = h_j - p_j/\rho_j$ and $U_r = C_r(T - T_{\mathrm{ref}})$, where C_r is the rock volumetric heat capacity coefficient and T_{ref} is the reference temperature.

Additional local constraints are required to close the system of governing equations 1–3. Based on the assumption of instantaneous thermodynamic equilibrium of the fluid mixtures, we can write

$$f_{\mathrm{ij}}(p, T, x_{\mathrm{ij}}) - f_{\mathrm{ik}}(p, T, x_{\mathrm{ik}}) = 0, \quad \forall j \neq k = 1 \ldots n_p, i = 1 \ldots n_c. \tag{4}$$

Here, we assume that all components can dissolve in all fluid phases, and that the capillary pressure has a negligible impact on the phase behavior [60, 68].

The system is supplemented with linear constraints for the phase compositions and the phase saturations, namely

$$\sum_{j=1}^{n_p} S_j = 1, \tag{5}$$

$$\sum_{i=1}^{n_c} x_{\mathrm{ij}} = 1, \quad j = 1 \ldots n_p. \tag{6}$$

Equations 1–6 describe the multiphase thermal-compositional flow problem. We use a generalized natural variables formulation [11] and base the phase behavior on the volume-translated Soave–Redlich–Kwong equation of state (EOS) [48]. Accurate determination of the phase state in a control volume (gridblock) is critical for efficient compositional simulation, and for that purpose, we use the multiphase bypassing strategy [69].

2.2 Mechanical deformation

We use the term thermo-poro-plasticity to refer to macroscale models of fluid-structure interactions in the plastic regime in the presence of thermal gradients; specifically, we consider locally homogeneous aggregates of the solid skeleton and the pore fluids [44]. We assume that in the liquid phase the average stress is identical to the pressure; the concept of the equivalent pressure is described in [12]. The second part of the total stress is the effective stress, which transmits forces between grain contacts. A quasi-static momentum conservation equation for an aggregate (skeleton plus pore fluids) can be written as:

$$\nabla \cdot \boldsymbol{\sigma} + \rho g = 0, \tag{7}$$

where $\rho = \rho_s(1-\phi) + \rho_f \phi$ is the overall mass density. Here, ρ_s is the density of the solid skeleton and ρ_f is the average fluid density. The symmetric total stress tensor $\boldsymbol{\sigma}$ contains the contributions of both the fluid and the solid skeleton [12]:

$$\boldsymbol{\sigma} = \mathbb{C}\boldsymbol{\epsilon}^e - \mathbf{b}P. \tag{8}$$

Here, $\mathbb{C}$ is the fourth-order elasticity-moduli tensor, $\boldsymbol{\epsilon}^e$ is the second-order elasticity strain tensor, and $b\underline{\mathbf{1}}$, where b is Biot's coefficient. The average fluid pressure is defined as $P = \sum_{j=1}^{n_p} S_j p_j$.

We follow the "small deformation" theory and assume that the total strain tensor, $\boldsymbol{\epsilon}$, can be decomposed into three parts: elastic, plastic, and thermal, which we write as

$$\boldsymbol{\epsilon} = \boldsymbol{\epsilon}^e + \boldsymbol{\epsilon}^p + \boldsymbol{\epsilon}^\theta, \tag{9}$$

The elastic strain can be expressed as

$$\boldsymbol{\epsilon}^e = \boldsymbol{\epsilon} - \boldsymbol{\epsilon}^p - \boldsymbol{\epsilon}^\theta. \tag{10}$$

We assume that the dilation induced by temperature is isotropic, i.e.,

$$\boldsymbol{\epsilon}^\theta = \alpha T \underline{\mathbf{1}} \tag{11}$$

where α is the skeleton linear thermal expansion/dilation coefficient [12]. Combining Eq. 9 and Eq. 8, we obtain

$$\boldsymbol{\sigma} = \mathbb{C} \cdot \left(\boldsymbol{\epsilon} - \boldsymbol{\epsilon}^p\right) - \mathbf{a}T - \mathbf{b}P, \tag{12}$$

where $\mathbf{a} = \alpha \mathbb{C} \underline{\mathbf{1}}$.

To complete the description, we define the total strain as

$$\boldsymbol{\epsilon} = \frac{1}{2}\left(\nabla u + \nabla^T u\right), \tag{13}$$

where u is the displacement vector. We use the Drucker–Prager [16] model to describe the stress–strain response in Eq. 12. To describe the plastic behavior, the classic Drucker–Prager model employs the following yield surface $\mathcal{F}$:

$$\mathcal{F} = \sqrt{J_2} + B \cdot I_1 + A, \tag{14}$$

where I_1 and J_2 are the volumetric and deviatoric invariants of the effective stress, respectively, and A and B are material parameters. We assume that the Drucker–Prager model circumscribes the Mohr-Coulomb yield surface, and we consequently express A and B as

$$A = \frac{6c\cos\psi}{\sqrt{3}(3-\sin\psi)}, \quad B = \frac{2\sin\psi}{\sqrt{3}(3-\sin\psi)}, \tag{15}$$

where ψ is the internal friction angle, and c is the cohesion. This model is intended to capture plastic dilation, and the size of the yield surface is controlled by "internal state" variables, such as softening and hardening parameters. In this paper, we employ an isotropic softening/hardening rule which is given in rate form and reflects the change of the cohesion as a function of the volumetric plastic strain and temperature changes (see A for details):

$$\dot{c} = H_v \dot{\epsilon_v^p} - H_t \dot{T}. \tag{16}$$

Here, H_v and H_t are two material parameters, $\epsilon_v^p = \mathrm{tr}\,(\epsilon^p)$ is the volumetric plastic strain. The Drucker–Prager model belongs to a class of "time-independent" plasticity models, and that the dot denotes the rate, i.e., change between loading steps. Specifically, the dot indicates a derivative with respect to a pseudo-time variable that characterizes the deformation rate. The first term on the right-hand side of Eq. 16 allows the yield surface to grow with plastic volumetric compaction (hardening) and shrink with plastic dilation (softening). The second term controls the shrinking of the yield surface caused by a temperature increase.

Following [12], we introduce the porosity as the ratio of the volume of the connected pore space to the total volume, and we use the following relationship between the porosity and stress/strain:

$$\begin{aligned}\phi - \phi^p &= \phi_o + \frac{(b-\phi_o)(1-b)}{K_d}(P - P_o) \\ &\quad + b\left(\epsilon_v - \epsilon_v^p\right) - \alpha_\phi\left(T - T_o\right).\end{aligned} \tag{17}$$

Here, K_d is the local drainage bulk modulus, $\epsilon_v = \mathrm{tr}\,(\boldsymbol{\epsilon})$ is the volumetric total strain, and α_ϕ is the volumetric thermal dilation coefficient related to the porosity. The reference porosity, pressure, and temperature are denoted as ϕ_o, P_o, and T_o, respectively. Assuming that the irreversible porosity is defined as $\phi^p = b\,\epsilon_v^p$, we obtain

$$\begin{aligned}\phi &= \phi_o + \frac{(b-\phi_o)(1-b)}{K_d}(P - P_o) \\ &\quad + b\epsilon_v - \alpha_\phi\left(T - T_o\right).\end{aligned} \tag{18}$$

We use a simple model for the permeability [14]:

$$k = k_o\left(\frac{\phi}{\phi_o}\right)^m. \tag{19}$$

The permeability exponent, m, describes how the permeability deviates from the reference value k_o.

The coupled set of equations is supplemented with initial and boundary conditions. The initial distribution of the fluids, pressure, temperature, and stresses are specified to fully define the initial state of the reservoir. Specification of the boundary conditions for the coupled problem can be quite challenging. Two types of boundary conditions are normally used for the flow equations: the prescribed pressure, temperature and prescribed flux. The mechanical-equilibrium equations use stress and displacement boundary conditions. Care is taken to ensure that the initial and boundary conditions provide a consistent set for the coupled flow-mechanics problem of interest. The Saint-Venant's principle is commonly used to correctly specify the boundary conditions. The principle states that the stress concentration is a relatively local phenomenon and becomes small at sufficiently large distances from the load. Consequently, mechanics boundary conditions must be applied on sufficient distance from the reservoir to obtain reasonably accurate results.

3 Solution strategy

We combine the finite-volume method, which is widely used in the reservoir simulation community [4], and the finite-element method, which is widely used in the civil

and mechanical (geotechnical) engineering communities [73]. The flow variables $R = (p, T, x)$ (pressure p, temperature T, and phase compositions x) are associated with cell centers, and the mechanics variables $U = (\boldsymbol{u}, \boldsymbol{\epsilon}^p)$ (incorporating displacement u and plastic strain $\boldsymbol{\epsilon}^p$) are associated with vertices and integration points [26, 30]. This combined finite-volume/finite-element formulation leads to a set of coupled nonlinear equations that are solved using either FI or SI methods. To determine the plasticity component of the total deformation, we apply the general closest point projection algorithm [56].

In the FI scheme, the mass, energy, and momentum conservation equations (cast in residual form) are solved simultaneously. The corresponding system of nonlinear algebraic equations is solved using Newton's method with safeguarding; in the FI strategy, each Newton iteration entails solving a linear system with the full Jacobian matrix.

The second approach is the SI method, in which we partition the overall multi-physics problem into sub-problems. The nonlinear sub-problems are then solved in a particular sequence. The SI strategy entails prescribing the specific solution sequence of the sub-problems and the details of the nonlinear operator splitting.

We employ the fixed-stress scheme as the nonlinear splitting SI strategy. This scheme enjoys unconditional stability for nonlinear poro-elasticity and does not exhibit oscillations in time [30]. The solution (R, U) is obtained incrementally by performing a sequence, such as

$$\begin{aligned} R_{k+1} &= R_k + \Delta R\left(R_k, U_k\right), \\ U_{k+1} &= U_k + \Delta U\left(R_{k+1}, U_k\right), \end{aligned} \tag{20}$$

where k and $k+1$ are the iteration indices.

The core idea of the fixed-stress split is the assumption that the mean total stress $\sigma_m = \mathrm{tr}\left(\boldsymbol{\sigma}\right)/3$ does not change between coupling iterations k and $k+1$:

$$\sigma_{m,k+1} - \sigma_{m,k} = 0. \tag{21}$$

Furthermore, we assume that the total stress increment can be expressed in terms of the primary variables as [29]:

$$\begin{aligned} \sigma_{m,k+1} - \sigma_{m,k} = K_d \cdot \left(\boldsymbol{\epsilon}_{v,k+1} - \boldsymbol{\epsilon}_{v,k}\right) - b\left(P_{k+1} - P_k\right) \\ - A_d\left(T_{k+1} - T_k\right), \end{aligned} \tag{22}$$

where the coefficients K_d and A_d have been introduced. The remarks below explain the choice of K_d and A_d. Using Eq. 21, the increment of $\boldsymbol{\epsilon}_v$ becomes a function of the pressure and temperature change:

$$\boldsymbol{\epsilon}_{v,k+1} - \boldsymbol{\epsilon}_{v,k} = \frac{b}{K_d}\left(P_{k+1} - P_k\right) + \frac{A_d}{K_d}\left(T_{k+1} - T_k\right). \tag{23}$$

Equation 18 at iteration $k+1$ is

$$\begin{aligned} \phi_{k+1} = \phi_o + \frac{(b-\phi_o)(1-b)}{K_d}\left(P_{k+1} - P_o\right) \\ + b\epsilon_{v,k+1} - \alpha_\phi\left(T_{k+1} - T_o\right). \end{aligned} \tag{24}$$

Substituting Eq. 23 into Eq. 24, we obtain

$$\begin{aligned} \phi_{k+1} = \phi_o + \frac{(b-\phi_o)(1-b)}{K_d}\left(P_{k+1} - P_o\right) \\ + b\epsilon_{v,k} - \alpha_\phi\left(T_{k+1} - T_o\right) \\ + \frac{b^2}{K_d}\left(P_{k+1} - P_k\right) + b\,\frac{A_d}{K_d}\left(T_{k+1} - T_k\right), \end{aligned} \tag{25}$$

where the last two members are the fixed-stress correction terms. Details of the implementation of the FI and SI schemes are given in the Appendix A. The specific choice of the parameter, K_d, in Eq. 25 has an impact on the rate of convergence.

For general three-dimensional elasticity problems, we use the Voigt bulk modulus (see [9, 28] for other possible choices):

$$K_d \approx \frac{1}{9}\underline{\mathbf{1}}^T \mathbb{C}\underline{\mathbf{1}}, \tag{26}$$

$$A_d \approx 3\alpha K_d, \tag{27}$$

where α is the skeleton linear thermal expansion/dilation coefficient [12], and $K_d \approx \dfrac{E}{3\left(1-2\nu\right)}$ for isotropic linear elastic material.

In elasto-plasticity simulations, K_d is obtained using the elasto-plastic moduli, i.e., the tensor $\mathbb{C}$ in Eq. 26 is replaced by $\mathbb{C}^{\mathrm{ep}}$. It has been shown that the moduli tensor, $\mathbb{C}^{\mathrm{ep}}$, can be taken from the previous sequential step [28]. The coefficient A_d is calculated from the expression $A_d = \mathrm{tr}\left(\mathbf{a}^{\mathrm{ep}}\right)/3$, where the elasto-plastic thermal moduli, $\mathbf{a}^{ep}$, are similarly taken from the previous sequential step. This choice of K_d and A_d greatly simplifies the overall algorithm, because it enables us to avoid return-mapping steps during the solution of the flow problem. Detailed derivations of $\mathbb{C}^{\mathrm{ep}}$ and $\mathbf{a}^{ep}$ are given in Appendix A.

4 Numerical examples

In this section, we demonstrate the applicability of the proposed framework to multi-physics problems of practical interest. We use five test cases for this purpose . The first three cases are used to compare our numerical results with available analytical and numerical benchmarks. The fourth case demonstrates that the sequential approach can accurately solve a highly nonlinear flow-thermal-geomechanics problem. The fifth case is designed to compare the performance of SI and FI schemes for a set of flow-geomechanics problems of different complexity.

4.1 Thermo-elastic consolidation of a sand column

We consider the thermo-elastic consolidation problem introduced by [1], which has been widely used as a benchmark

[34, 45]. In this example, a one-dimensional (1D) column of height 7 m and width 2 m is subjected to a compressive load force of 100 kPa on its top boundary (see Fig. 1). The zero vertical displacement condition constrains the bottom and side boundaries, which are impermeable (no-flow). The pressure and temperature on the top boundary are fixed and equal to 0 Pa and 323.15 K, respectively. The column is saturated with a single-phase fluid, and the fluid pressure and temperature are equal to 1 Pa and 273.15 K, respectively. Table 1 lists the parameters of this test case. Following [45], the fluid compressibility, thermal expansivity, viscosity variation, and gravity effects are assumed to be negligible.

Figure 2 shows the vertical displacement at $(x = 0, z = 0)$. The numerical solution obtained by FI strategy is in close agreement with published reference (see Fig 2). FI and SI schemes give the same results.

4.2 Mandel problem

The second case is the two-dimensional (2D) Mandel consolidation problem [39]; the analytical solution of which is widely used as an important benchmark for the numerical solution of poromechanics problems. A more detailed description may be found in [12]. The computational domain is defined as $\Omega = [0, a] \times [0, b] = [0, 20\text{ m}] \times [0, 10\text{ m}]$; the geometry represents a quarter of the original Mandel problem (see Fig. 3). The domain is fully saturated with a compressible single-phase fluid, and the initial fluid pressure is $p_{\text{init}} = 44.17 \cdot 10^5$ Pa. We impose no-flow boundary conditions everywhere except on the right boundary, where a constant pressure $p|_{x=a} = 0$ is prescribed. The main model parameters are given in Table 2.

We set the horizontal displacement on the left boundary and the vertical displacement on the bottom boundary to zero ($u_x|_{x=0} = 0$, $u_z|_{z=0} = 0$), and we apply uniform loading conditions on the top boundary ($F|_{z=b} = 100 \cdot 10^5$ Pa). The vertical displacement on the upper boundary is constrained by the condition that $u_z|_{\forall x}$=constant. The undrained Poisson ratio is used to initialize the displacement field, and the drained Poisson ratio is used for the transient period.

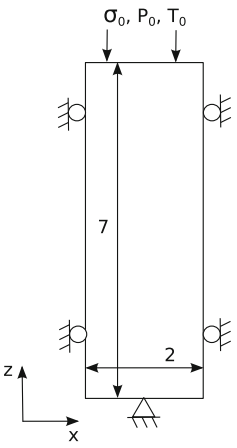

Fig. 1 Geometry and boundary conditions of the thermo-elastic consolidation problem

Table 1 Rock and fluid properties used for the thermo-elastic consolidation problem

Property	Value
Porosity ϕ, %	25
Hydraulic conductivity $(k\rho_f g/\mu_f)$[a], m/s^2	$4 \cdot 10^{-6}$
Young's modulus E, Pa	$6 \cdot 10^3$
Biot's constant b	1
Poisson's ratio ν	0.25
Linear thermal expansion α, 1/K	$3 \cdot 10^{-6}$

[a] k permeability, ρ_f fluid density, μ_f fluid viscosity, g gravitational acceleration

The pressure evolution at $(x = 0, z = 0)$ is shown in Fig. 5. Both the SI and FI approaches accurately capture the transient pressure behavior. This example shows that the SI method has the same accuracy as the FI approach, and that it converges within 3–20 iterations with a tolerance of $\varepsilon = 10^{-6}$ (Fig. 4). The convergence rate for the SI scheme is consistent with published results [9], where the maximum number of iterations per time step was estimated to be 10 for a tolerance of $\varepsilon = 10^{-3}$.

4.3 Depletion of a box-shaped reservoir

Next, we study Dean's test problem [15]. The simulation domain is a box of size $\Omega = 18897.6\text{ m} \times 9448.8\text{ m} \times 3429.0\text{ m}$ containing three layers: top layer (0–3048 m), middle layer (3048–3124.2 m), and bottom layer (3124.2–3429.0 m). The payzone of the reservoir, $\Omega_r = 6705.6\text{ m} \times 3352.8\text{ m} \times 76.2\text{ m}$, is located in the middle layer. The

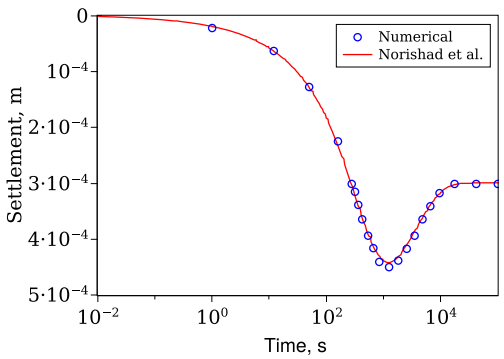

Fig. 2 Thermo-elastic consolidation problem is top surface settlement. Solid lines represent the numerical solution obtained by FI strategy; circles show reference values

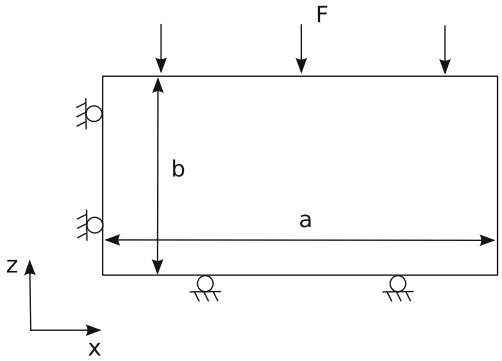

Fig. 3 Geometry and boundary conditions of Mandel problem

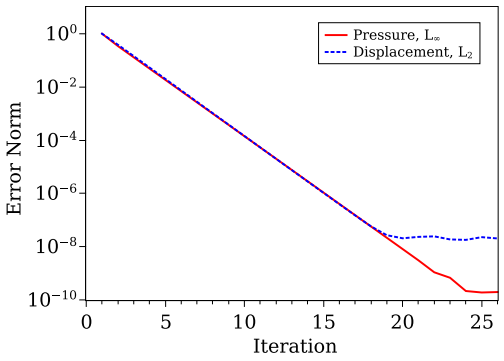

Fig. 4 Mandel's problem with the SI convergence profile after first time step, $\delta t = 0.00115$ days. Within 15 coupling iterations, both the L_∞ and L_2 errors decrease below the tolerance of $\varepsilon = 10^{-7}$

payzone has the same thickness as the middle layer and is surrounded by a stiff impermeable medium. Figure 6 shows a geometrical configuration of the model, and Table 3 lists the rock properties.

The "pay" and "non-pay"zones are fully saturated with a single-phase liquid with a density of 1000 kg/m^3 at 10^5 Pa, a compressibility of $3 \cdot 10^{-10}$ Pa^{-1}, and a viscosity of 10^{-3} Pa s. The initial fluid pressure is 10^5 Pa at the surface with a hydrostatic gradient of $0.98852022 \cdot 10^5$ Pa/m; the initial vertical stress is 0 Pa at the surface with a vertical stress gradient of $0.9869 \cdot 10^5$ Pa/m, and the initial horizontal stresses are half of the vertical stress. The bottom and side boundaries are constrained to have zero normal displacement. The wellbore with a radius 0.0762 m is located in the center of the domain and fully penetrates the payzone. The well operates at a constant production rate of 7949.365 m^3/day for a period of 4000 days.

We plot the pressure behavior at the top boundary of the reservoir (top right corner of the dark box in Fig. 7). We also plot the subsidence at the top of the reservoir and at the surface. We then compare the simulation results with the published solution [15]. As Fig. 7 indicates, there is a good match. Owing to the Mandel–Crayer effect, the pressure increases in the early stages, reaches a maximum value, and then monotonically decreases (see Fig. 7 (left)). Dean's results are reproduced using the FI and the SI schemes.

Table 2 Rock and fluid properties used for Mandel's problem

Property	Value
Reference porosity ϕ_o, %	20
Young's modulus E, Pa	$1 \cdot 10^9$
Biot's constant b	1
Poisson ratio ν	0.25
Undrained Poisson ratio ν_u	0.47
Permeability k, mD	1
Fluid viscosity μ_f, Pa · s	$9.81 \cdot 10^{-5}$
Fluid compressibility C_f, Pa^{-1}	$2 \cdot 10^{-10}$
Reference fluid density ρ_f, kg/m^3	1000

4.4 Modeling of SAGD with geomechanics

The steam-assisted gravity grainage (SAGD) process is a widely used recovery technique for heavy oil (bitumen) reservoirs [7, 35]. The process involves complex multi-physics nonlinear interactions, such as fluid thermal expansion, rock thermal dilation, and complex phase behavior. Typical SAGD operations involve the location of a pair of horizontal wells, one a few meters above the other [7]. Steam is injected into the upper well to form a steam chamber and mobilize the reservoir oil, which drains into the lower production well. However, the significant mechanical stresses associated with SAGD operations can increase the risk of fracturing the reservoir or the caprock. Numerical simulation of SAGD problems is extremely difficult because the evolution entails large and highly nonlinear variations in composition, phase state, densities, and viscosities as a function of temperature and pressure. In the SAGD process, the injected steam has much lower viscosity and higher phase mobility than the resident heavy oil, and we have to deal with severe temperature gradients. Moreover, typical bitumen sandstone formations exhibit nonlinear deformation characteristics, and that makes the fluid-structure interactions quite complex. Here, we study the behavior of both FI and SI-based solution schemes for a SAGD problem that is broadly representative of Athabasca sands [36, 50].

We have previously reported on numerical simulation of SAGD problems using the fully implicit scheme for thermal-compositional problems [60, 68] and for thermo-compositional-geomechanical problems [21]. Here, we compare the performance for three coupling strategies FI, SI, and what we refer to as single-pass SI, whereby one outer iteration of the SI scheme is used. The single-pass SI scheme is cheaper than FI and SI, and is often used because it minimizes the data transfer operations when two different

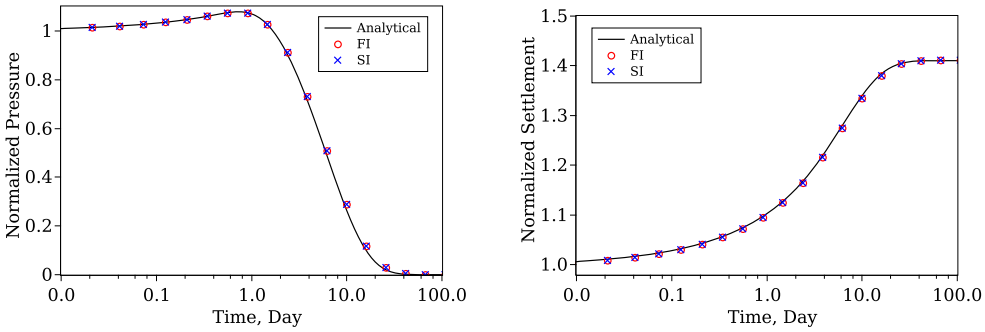

Fig. 5 Mandel's problem with the comparison of the analytical and numerical solutions of the pressure at ($x = 2.5, z = 0$) and vertical settlement at ($x = 0, z = 100$). The solid line represents the analytical solution, and the symbols represent the FI and SI solutions

simulators (one for fluid flow, one for mechanics) are used to solve the problem.

We use the description of the SAGD model provided in [21, 60]. The simulation domain contains four layers (Fig. 8): the first layer (0–155 m) represents a clear water formation, the second layer (155–180 m) is caprock, the third layer (180–205 m) is an oil sand reservoir, and the fourth layer (205–350 m) is bedrock. The model dimension in Y direction is 800 m. We assume that the caprock and the bedrock are almost impermeable, and that the permeability and porosity of the third layer is high, i.e., $k = 2000$ mD and $\phi = 32\%$, respectively. The thermal conductivity is constant for all layers. The production layer is fully saturated with heavy oil and water containing four components: methane, propane, heavy oil, and water. A detailed description of the fluid properties and the phase behavior can be found in [60].

We use the Drucker–Prager model [16] to describe the nonlinear mechanical properties of the bitumen-sand formation. In this case, the caprock and the bedrock are assumed to have elastic responses. The main model parameters are given in Table 4.

The boundary conditions are shown in Fig. 8. The displacements on the vertical and bottom sides are fixed, whereas the top boundary is loaded by the atmospheric pressure. All the boundaries are impermeable to flow. The initial pressure and temperature distributions are shown in Fig. 9.

Heavy oil (bitumen) is recovered from the production well at a depth of 203 m, and the injection well is located at a depth of 198 m. We consider two production stages. The first stage is preheating and lasts for 180 days; electric downhole heaters are used to deliver thermal energy to the formation. The heaters operate at a constant temperature of $T_{\text{bhp}} = 485$ K. The second stage is the injection stage, which entails the injection of saturated steam of (quality 95%) at a pressure of $P_{\text{bhp}} = 20 \cdot 10^5$ Pa, and a temperature of $T_{\text{bhp}} = 485$ K. The producer operates at a constant liquid rate of 48 m^3/day.

Given the symmetry of the model, we simulate only half of the reservoir. The computational domain is discretized using 4930 hexahedral elements. The mesh is refined near the production and injection wells. We use a simple timestep control scheme [4] with maximum changes in pressure $\Delta P = 10^5$ Pa and temperature $\Delta T = 10$ K per time step. Note that the average Courant–Friedrichs–Lewy (CFL) value for this problem is above 300, and this adds a

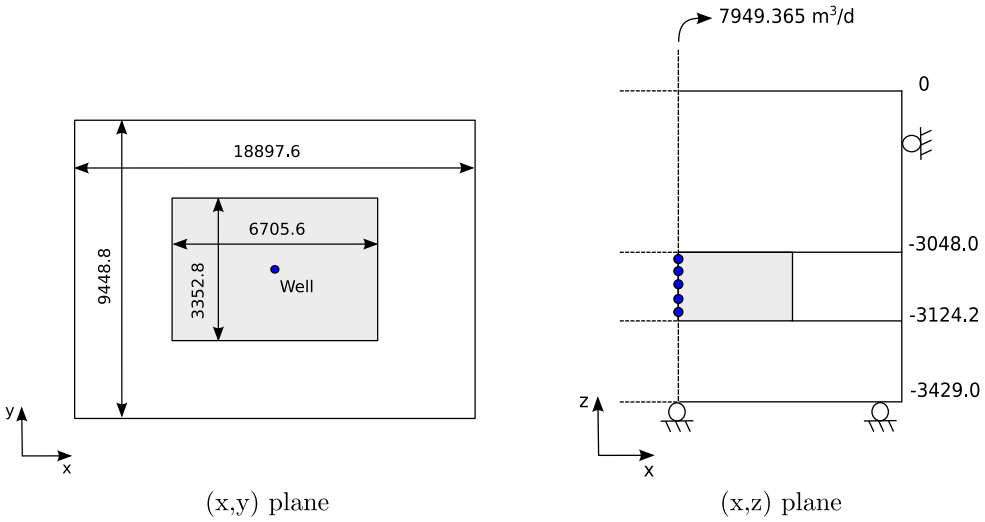

Fig. 6 Geometry of Dean's model

Table 3 Rock properties for Dean's model

Property	Reservoir	Nonpay zones
Porosity ϕ, %	25	25
Horizontal permeability k_h, mD	100	0
Vertical permeability k_v, mD	10	0
Young's modulus E, Pa	$0.0689476 \cdot 10^9$	$6.89476 \cdot 10^9$
Biot's constant b	1	1
Poisson ratio ν	0.25	0.25
Rock density ρ_r, kg/m^3	2700	2700

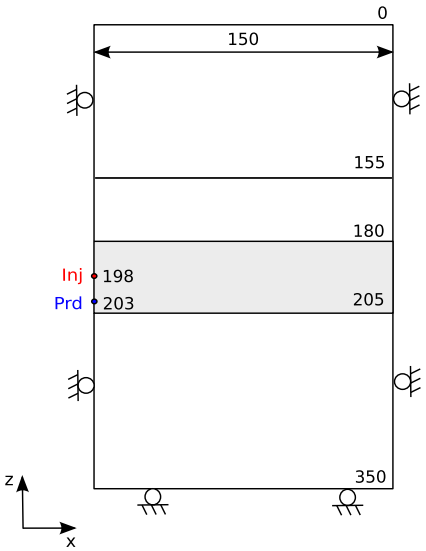

Fig. 8 SAGD model geometry. Coordinates: injector (0, 203), producer (0, 198)

"realistic" level of difficulty to the simulations. Because of the highly nonlinear interactions, we start with analyzing the FI approach results and use it as the reference solution strategy.

During the preheating stage, the temperature increases around the injection and production wells, leading to a decrease in the bitumen viscosity in those regions. At the end of the preheating period, the drop in bitumen viscosity allows the injection of steam and the production of the heated lower viscosity oil (see Fig. 10a,b). The temperature propagation changes the pressure distribution due—in part—to the thermal expansion of the fluids and rock. The changes in the pressure extend beyond the reservoir, and this is associated with the different thermal expansion characteristics of the rock and the fluids in the system. In general, the thermal energy injected into the system leads to changes in the rock and liquid volumetric responses and the pressure distribution in the reservoir; however, the very-low permeability of the caprock and the bedrock inhibits the propagation of the pressure leading to an increase in pressure, especially in regions close to the reservoir boundaries.

In our model, the bitumen-sand reservoir has a plastic response, whereas the caprock and bedrock have an elastic response. In addition, the caprock and bedrock are almost impermeable. During the active injection-production second stage, the overall pore pressure and the rock and oil temperatures increase and that leads to dilation of the rock skeleton (Fig. 10c). These changes can drive the system toward the plastic regime in parts of the reservoir. The simulation results show that plastic zones appear near the well and close to the reservoir boundary (Fig. 10d). Moreover, the Young's modulus of the reservoir is smaller, and lateral deformation of the reservoir is higher than the deformation of the bedrock and the caprock. In our example, lateral deformation is mostly driven by lateral pressure gradients. This explains the appearance of excessive stresses on the boundary, which, in turn, lead to the appearance of the plastic zones (Fig. 10d). Note that the use of adaptive time stepping strategies in the simulation of SAGD processes [60] may lead to small differences between the results obtained using different nonlinear solution schemes. We avoid this by applying the following procedure: (1) run the fully implicit simulation with the operation controls described above, (2) extract the steam-injection rates and the corresponding time steps, and (3) use this information as inputs for all the other simulations using different coupling strategies. Figure 11 shows the well controls.

The quality of the numerical solutions is analyzed using the spatial distribution of the errors for the flow and

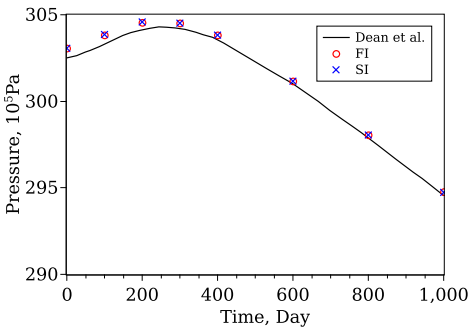

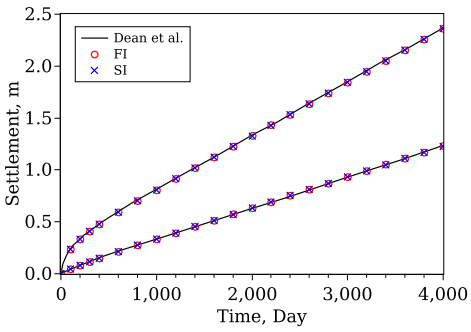

Fig. 7 Comparison of the simulations with Dean's solution. Left: pressure at cell (6, 11, 6). Right: settlement at (0, 0) m (top curve) and (0, 3048) m (bottom curve). The solid line represents the reference solution [15], and symbols represent the FI and SI results

Table 4 SAGD model parameters used in numerical simulations

Parameter	Layer 1	Layer 2	Layer 3	Layer 4
Porosity ϕ, %	0.4	0.1	0.32	0.1
Permeability (vertical) k_h, mD	0.01	0.1	2000	0.01
Permeability (horizontal) k_v, mD	0.01	0.1	1000	0.01
Thermal conductivity κ, W/ (m · K)	1.37	1.37	1.37	1.37
Volumetric heat capacity C_r, kJ/ $\left(\text{m}^3 \cdot \text{K}\right)$	2000	2000	2000	2000
Biot's coefficient b	1	1	1	1
Young's modulus E, 10^9 Pa	0.5	1.2	0.8	5
Poisson's ratio ν	0.13	0.15	0.3	0.3
Cohesion c, Pa	—	—	0	—
Friction angle ψ, deg	—	—	32	—
Rock density ρ_r, kg/m^3	2250	2250	2250	2250
Linear thermal expansion α, 10^{-5} 1/K	2	2	2	2
Pore thermal expansion α_ϕ, 10^{-5} 1/K	5.4	5.4	4.08	3.6
Thermal softening H_t, Pa/K	—	—	0	—
Plastic hardening H_v, Pa	—	—	0.25 K*[a]	—

[a] $K^* = E/\left(3\left(1-2\nu\right)\right)$

mechanics parts (Fig. 12). Obviously, compared with SI, the single-pass SI strategy has larger errors for both the flow and mechanics variables. Interestingly, the distribution of errors is not localized with significant differences throughout the computational domain.

It is important to note that the average CFL value for this problem is greater than 300, and the coupling strength τ for the layer with the highest error is estimated to be around 25. Nevertheless, the SI scheme shows good agreement with the FI scheme, and nonlinear convergence is achieved in 4–7 iterations with a tolerance of $\left(\varepsilon_f, \varepsilon_m\right) \leq 10^{-4}$.

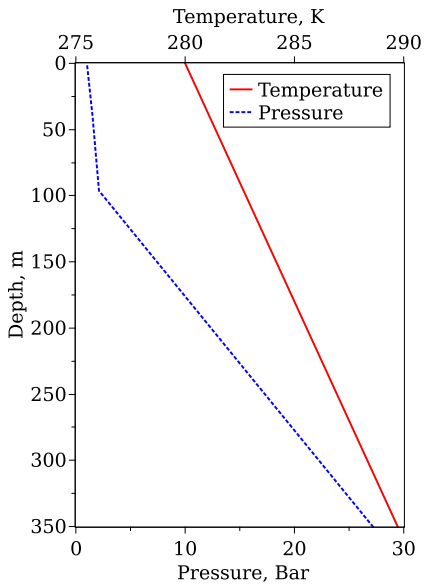

Fig. 9 SAGD problem initial pressure and temperature profiles

However, 12–15 iterations are needed to achieve a tighter tolerance of 10^{-7}. The single-pass SI scheme has errors of up to 12%. Similar convergence behaviors have been observed in the thermo-hydro-mechanical simulations of source-rock thermal maturation in [22]. For the problem considered here, it is clear that the SI approach is much more accurate than the single-pass SI scheme after an acceptable number of coupling iterations. As this problem involves many components, such as multiphase flash, temperature dependent properties, and nonlinear mechanics, it is quite demanding to implement the FI scheme, and the SI approach appears to be quite attractive.

4.5 Water flooding problem

The previous subsection demonstrated that the SI approach is able to converge for highly nonlinear problems, although many coupling iterations are required between the sub-problems (see Algorithm 3 in A). The question then arises: how expensive are these iterations? The main purpose of this subsection is to compare the computational cost of the FI and SI solution strategies.

To demonstrate the applicability of the proposed framework to solve problems of practical interest and assess the performance of the sequential-implicit scheme, we consider a modified SPE 10 problem. This problem was originally designed to test and compare upscaling techniques [10]; however, the model means has been used to compare the robustness and efficiency of a wide range of reservoir simulation schemes. Usually, the most time-consuming part of the simulation involves solving the linear system. As mentioned above, the FI approach for

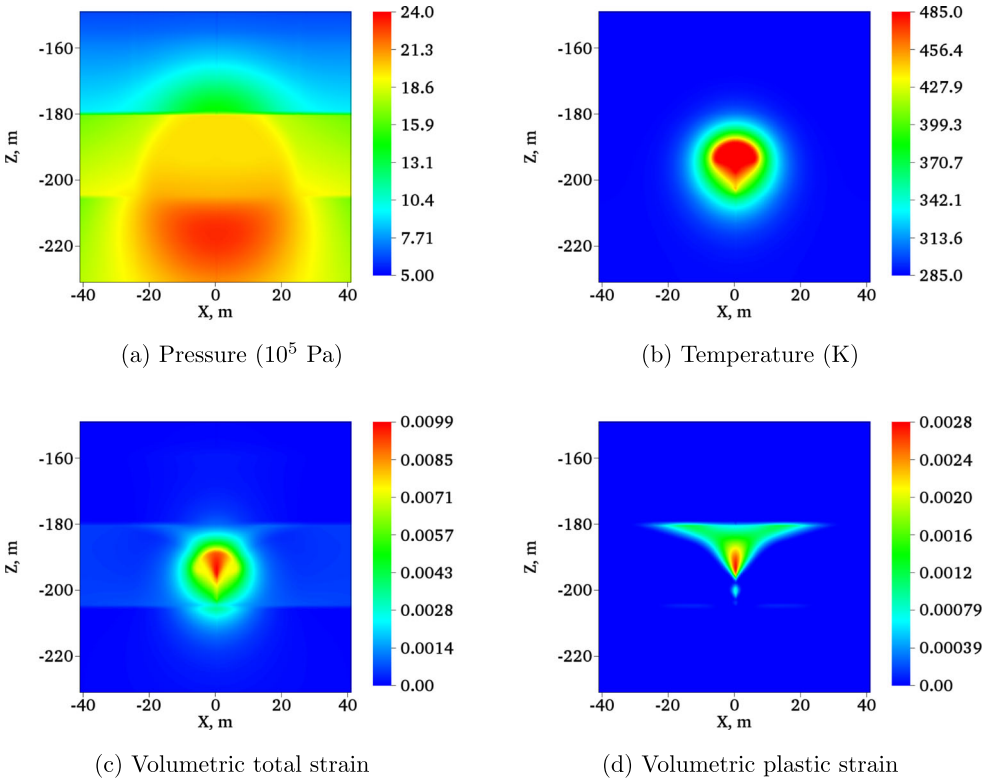

(a) Pressure (10^5 Pa) (b) Temperature (K)

(c) Volumetric total strain (d) Volumetric plastic strain

Fig. 10 SAGD problem solution at $t = 3$ years. The results obtained by FI strategy are shown

coupled geomechanical problems requires sophisticated linear solvers [64], and the choice of efficient solvers for large-scale problems is limited. For the following comparison, we employ our in-house iterative linear solver [32], which allows us to deal with the coupled problem in a fully implicit manner and enables a "fair" comparison of the FI and SI approaches within one platform.

The solver applies a multi-stage preconditioning strategy combining the generalized Constrained Pressure Residual (CPR) approach [70] with a fixed-stress strategy [64]. For the sequential scheme, we employ a CPR-preconditioned generalized minimal residual (GMRES) solver [70] to solve the flow problem, and an algebraic multigrid preconditioned GMRES solver to solve the geomechanical problem. We use the same convergence tolerance values for the FI and SI approaches.

In this study, we use the original SPE 10 dataset, including relative permeability curves, porosity and permeability distributions, fluid properties, and the well controls. The simulation domain $\Omega = 365.8\,\text{m} \times 670.6\,\text{m} \times 51.8\,\text{m}$ is discretized using a regular Cartesian grid into $60 \times 220 \times 85$ cells. The top 35 layers represent a formation with a permeability field that has a Gaussian distribution, and the bottom 50 layers are characterized by a channelized permeability field with high-contrast features. We generate a set of coarsened models, containing 24 960–399 360 cells (see Table 5), and we upscale the properties using a simple volume-averaging approach.

The original SPE 10 benchmark is a two-phase flow problem. We extend the model and define the geomechanical parameters. The extended model is supplemented by boundary conditions and parameters for the pore-mechanical

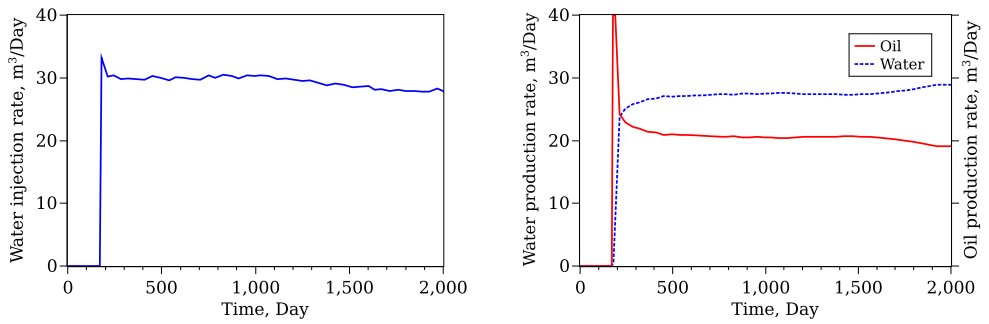

Fig. 11 Well-operation controls for SAGD problem: steam (cold-water equivalent) injection rate (left), water, and oil production rates (right)

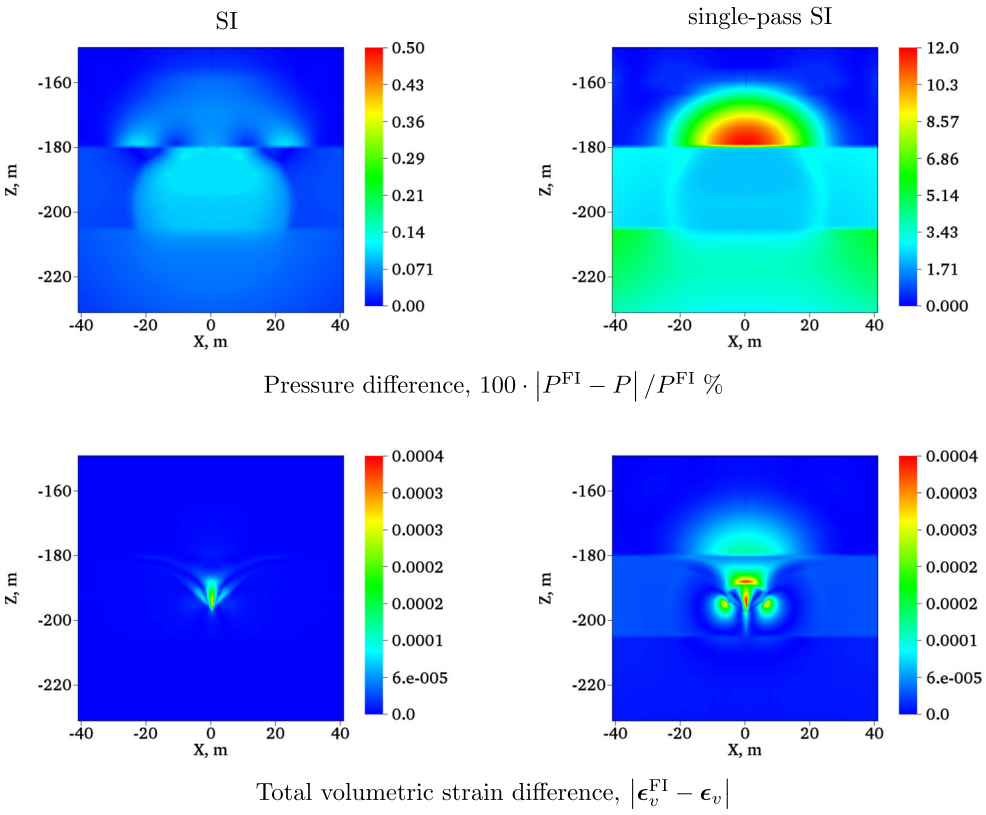

Fig. 12 SAGD problem: comparison of the SI (left) and single-pass SI (right) numerical solutions

problem. We set zero normal displacement on the side boundaries, zero vertical displacement on the bottom boundary, and uniform loading conditions on the top boundary, $F_{\mathrm{top}} = 900 \cdot 10^5$ Pa. The Biot's coefficient is set to 1.0, and the Poisson ratio is 0.2.

We use three different settings with different coupling strengths to study the performance of the sequential scheme. A detailed description of the coupling strength can be found in [31] and [9]. The baseline case uses the original rock compressibility value $c_r = 1.45 \cdot 10^{-10}$ Pa^{-1} to estimate the average Young's modulus $E_{\mathrm{av}} = 3\,(1-2\nu)\,/c_r$. The Young's modulus values are then distributed on the grid using the following correlation:

$$E_{1.0}(\boldsymbol{x}) = E_{\mathrm{av}} \cdot (a \cdot \phi(\boldsymbol{x}) + b), \tag{28}$$

where ϕ is the initial porosity and a, b are parameters chosen to obtain $\min(E_{1.0}) = E_{1.0}(\max(\phi)) = 0.2\,E_{\mathrm{av}}$ and $\max(E_{1.0}) = E_{1.0}(\min(\phi)) = 5\,E_{\mathrm{av}}$. Figure 13a illustrates the distribution of the Young's modulus. The second and third cases use softer and stiffer moduli: $E_{0.1} = 0.1\,E_{1.0}$ and $E_{10.0} = 10\,E_{1.0}$. The $E_{0.1}$ case corresponds to stronger coupling and the $E_{10.0}$ case corresponds to weaker coupling (when compared with the baseline). Figure 13b shows an example of the distribution of the coupling strength τ for the softer moduli case, $E_{0.1}$. As can be seen, τ reaches a fairly high value ($\sim$ 150), and consequently the SI strategy may require a high number of coupling iterations to converge. This test set allows us to investigate the performance of the sequential scheme for 15 different combinations of model resolution and coupling strength. In addition to the effect of the coupling strength between the flow and mechanics, we also investigate how the nonlinearities impact the overall performance. The simulation results are summarized in Table 6.

We start with modeling single-phase poromechanics. The domain is fully saturated with water ($S_w^{\mathrm{init}} = 1.0$). It has been shown [9] that the SI approach requires a larger number of iterations when the coupling is stronger. The case with $E_{10.0}$ has weaker coupling and the SI schemes converges in a relatively small number of iterations (Fig. 14); as a result, the SI scheme outperforms the FI scheme.

Table 5 Number of cells and total number of degrees of freedom (DOFs) for the simulation cases

Case name	25k	50k	100k	200k	400k
Number of cells	24 960	49 920	99 840	199 680	399 360
DOFs	134 667	267 735	522 555	1 037 235	2 068 395

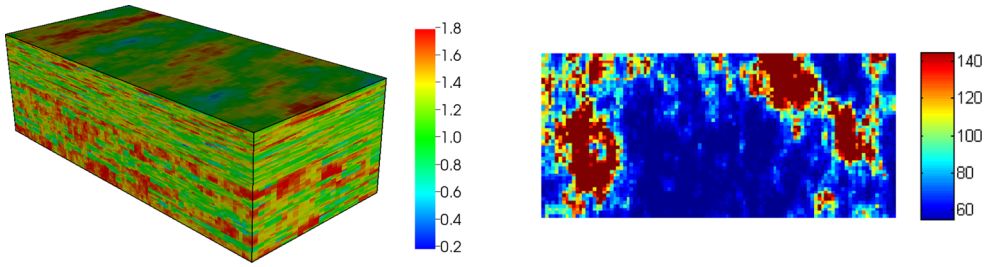

Fig. 13 Extended SPE 10 model. Reservoir domain $\Omega = [0, 250] \times [0, 500] \times [-3650, -3800]$ m. The top part is characterized by smoothly varying rock properties, whereas the bottom part has channelized distributions of the properties with long-correlation and high-contrast features. Young's modulus distribution for the case $E = E_{1.0} \cdot 10^{10}$ Pa (left) and the coupling strength τ distribution for the second layer of the model and $E = E_{0.1}$ (right)

Compared with the FI approach, the SI scheme performs comparably well for $E_{1.0}$ and is much slower for $E_{0.1}$. Overall, we have found that the convergence rate of FI is much less sensitive to the coupling strength compared with the SI approach. Since the nonlinearity in the problem is quite mild, the FI method requires 1–2 Newton iterations per time step to achieve convergence, and the overall performance of the FI scheme depends strongly on linear solver capabilities. Here, we employ a special-purpose multi-stage linear solver that exhibits robust and scalable performance; the details are described elsewhere [32]. On the other hand, the overall performance of the SI strategy depends strongly on the number of outer iterations (i.e., the number of times we solve a flow problem followed by a mechanics problem), which is quite sensitive to the coupling strength. Not surprisingly, we observe that FI outperforms SI when the number of SI iterations is large (see Fig. 17a).

Next, we consider two-phase problems (Fig. 15) using an initial water saturation $S_w^{\text{init}} = 0.2$. The porous medium still has linear-elastic deformation characteristics, whereas the flow problem is highly nonlinear. The FI approach requires multiple Newton iterations for convergence. Thus, with respect to the single-phase setup, the cost of the FI scheme increases because of the increased number of nonlinear (Newton) iterations. For the FI scheme, the average number of Newton iterations per time step increases by a factor of

Table 6 Normalized simulation time for the extended SPE 10 model

	$E_{0.1}$		$E_{1.0}$		$E_{10.0}$	
Case	FI	SI	FI	SI	FI	SI
Single-phase, elasticity						
25k	1.38	2.11	*1.00*	0.97	0.95	0.79
50k	3.09	4.95	2.32	2.12	2.15	1.70
100k	6.64	10.44	4.89	4.58	4.55	3.52
200k	15.47	26.49	10.38	10.58	9.17	7.38
400k	40.78	60.00	26.84	24.99	23.18	18.60
Two-phase, elasticity						
25k	1.21	1.31	*1.00*	0.54	1.00	0.40
50k	3.03	2.99	2.28	1.18	2.26	0.86
100k	6.79	5.75	5.40	2.60	5.48	1.86
200k	18.92	14.77	12.76	6.94	12.48	4.58
400k	57.01	43.12	33.23	16.41	31.75	10.54
Two-phase, plasticity						
25k	1.33	3.47	1.06	1.23	1.01	0.75
50k	3.02	7.40	2.23	2.32	2.15	1.67
100k	7.20	11.39	5.14	5.57	5.40	3.28

The FI simulation time for the smallest problem (marked in italics) is used to normalize the simulation time

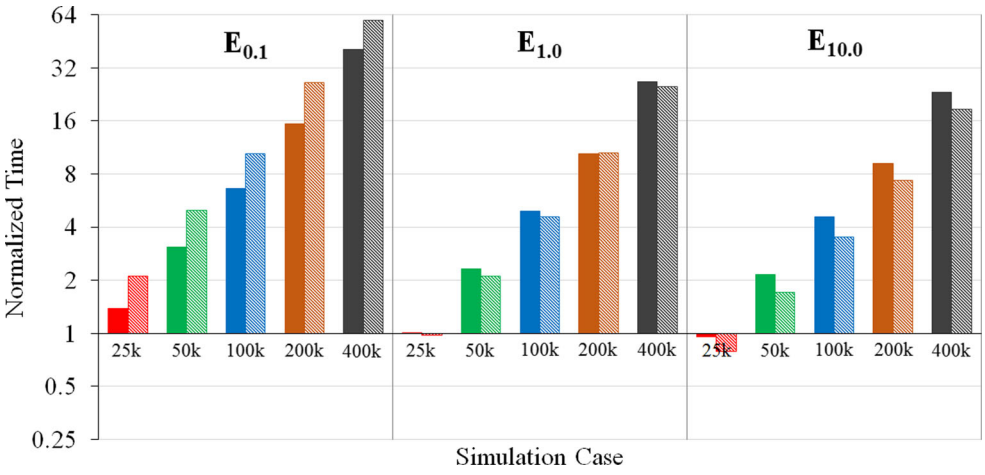

Fig. 14 Comparison of FI (solid color) and SI (dashed) simulation times for single-phase setup. Note the logarithmic scale on the vertical axis

more than eight compared with the single-phase flow case. In contrast, the number of sequential iterations increases by only a factor of 1.5. Moreover, the cost of solving of two implicit sub-problems is lower than solving the full problem. As a result (Fig. 17b), the SI approach is quite effective for this problem setup.

Now, we consider a two-phase flow problem with plastic mechanical deformation, so that both problems—flow and mechanics—are highly nonlinear. Here, the FI approach requires a similar number of nonlinear iterations as in the previous two-phase elastic setup (see solid bars in Fig. 16). However, the performance of the SI strategy is significantly degraded (dashed bars in Fig. 16). This is because the two nested nonlinear loops are performed for each coupling step (see Algorithm 3). As the coupling strength increases, the number of SI iterations increases dramatically, and that leads to poor performance compared with FI. For moderate and weak coupling, the sequential approach is quite competitive with FI approach (see Fig. 17c).

5 Summary

We presented a computational framework for the simulation of thermo-compositional-mechanics problems in subsurface porous formations. The thermo-compositional problem combines the nonlinear mass and energy conservation equations and the equations of state for thermodynamic equilibrium. We modeled the mechanical behavior of the rock using quasi-static geomechanical equations with

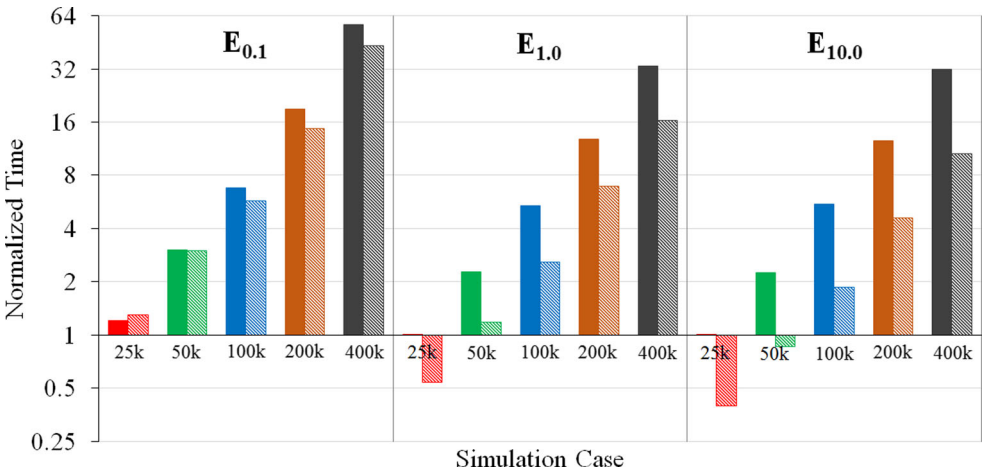

Fig. 15 Comparison of FI (solid color) and SI (dashed) simulation times for two-phase setup. Note the logarithmic scale on the vertical axis

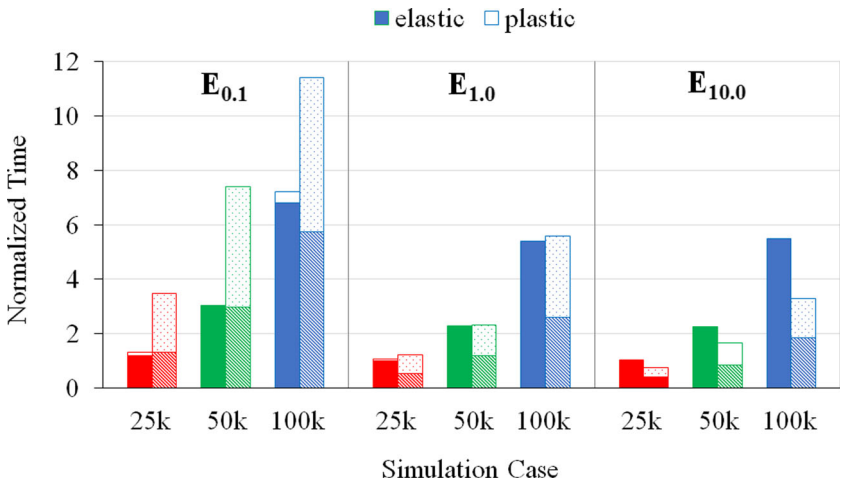

Fig. 16 Comparison of FI (solid) and SI (dashed) simulation times for the two-phase plastic setup. The light part of the bars corresponds to the increase in the simulation times for the elastic and plastic models

a plastic constitutive model. We used a finite-volume approximation for the thermal multi-component flow and a Galerkin finite-element approximation for the poro-thermo-plasticity. The resulting set of nonlinear equations was solved using FI and SI solution schemes. We studied the robustness and efficiency of the different schemes using available analytical and numerical benchmarks. In particular, we performed a comparison study of the SAGD recovery process. We showed that the model and the numerical schemes resolve the nonlinear coupling and the complex behavior related to steam-injection processes.

The results show that the FI strategy performs very well for coupled multiphase flow and geomechanics problems, but requires sophisticated development of the simulation framework (e.g., construction of full Jacobian matrices) and advanced multi-stage linear solvers. On the other hand, the SI-based strategies can be a viable alternative to FI-based simulators. We demonstrated that the sequential approach has predictable convergence behavior for complex problems with strong nonlinearities, whereby the cost is quite sensitive to the strength of coupling between the sub-problems. The SI approach also enables more freedom in the choice of linear and nonlinear solvers for each subproblem. Finally, the applicability of the sequential method is not limited to thermo-compositional-mechanical problems and can be extended relatively easily to a wide range of applications and multi-physics problems. Both FI and SI methods are implemented in a unified framework within the AD-GPRS research simulator, and that allows us to develop more complex models for future studies of multi-physics coupling strategies.

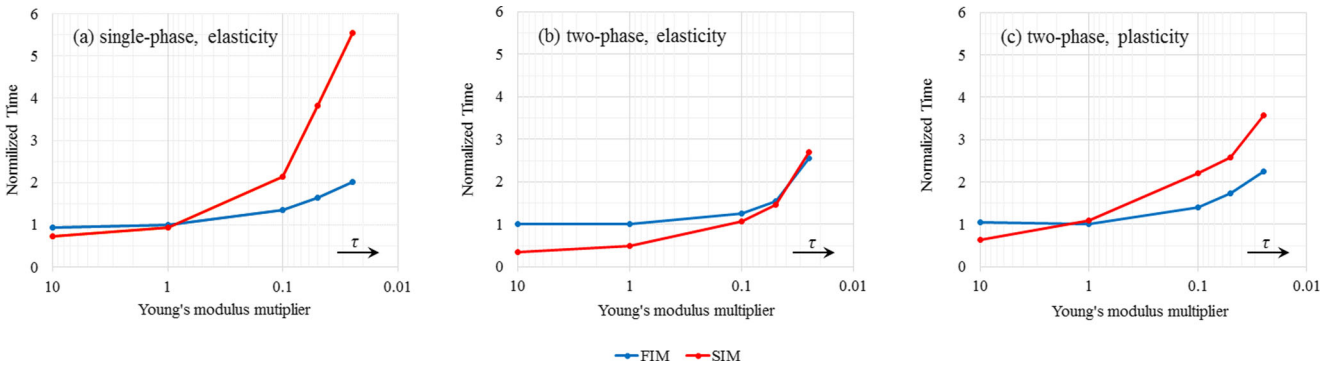

Fig. 17 Dependence of the normalized simulation time on the coupling strength. Smaller Young's modulus multiplier values correspond to stronger coupling between the flow and mechanical problems. Intermediate-size case 100k is chosen (see Table 5)

Funding information The authors gratefully acknowledge the financial support provided by the Reservoir Simulation Industrial Affiliates Consortium at Stanford University (SUPRI-B) and Total S.A. through the Stanford Total Enhanced Modeling of Source rock (STEMS) project.

Appendix A: Return-mapping algorithm

In this section, we describe the implementation of a return-mapping algorithm for the proposed plasticity model. We assume that the plastic flow potential function has the same form as the plastic yield function (associative plasticity) and consider isotropic hardening/softening behavior in the material of the payzone. For the plasticity, we use the Drucker–Prager model given by Eq. 14 with thermal softening and mechanical hardening. We use the General Closest Point Projection algorithm [56] to determine the plasticity components of the total deformation. The proposed thermo-plasticity model is given in terms of Biot's effective stresses $\boldsymbol{\sigma}'' = \boldsymbol{\sigma} + \mathbf{b}P$. Alternatively, the response can be formulated in terms of Terzaghi's effective stresses $\boldsymbol{\sigma}' = \boldsymbol{\sigma} + P$, and this formulation can be performed in the developed framework without significant modifications.

Using the total stress definition given in Eq. 12 and following [73], the plastic strain tensor rate is assumed to be given as a solution of the following system of equations:

$$\mathcal{F}\left(\boldsymbol{\sigma}'', c\right) = 0, \tag{A.1a}$$

$$\dot{\boldsymbol{\epsilon}^p} = \dot{\lambda}\frac{\partial \mathcal{F}}{\partial \boldsymbol{\sigma}''}, \tag{A.1b}$$

$$\dot{\boldsymbol{\sigma}''} = \mathbb{C}\cdot\left(\dot{\boldsymbol{\epsilon}} - \dot{\boldsymbol{\epsilon}^p}\right) - \mathfrak{a}\dot{T}. \tag{A.1c}$$

where a dot denotes the rate, i.e., the change between loading or time steps. Here, $\mathcal{F}$ is the yield function, λ is the proportionality constant, and $\mathfrak{a} = \mathbf{a} + \frac{\partial \mathbf{a}}{\partial T}\cdot T - \frac{\partial \mathbb{C}}{\partial T}\cdot\left(\boldsymbol{\epsilon} - \boldsymbol{\epsilon}^p\right)$. The system of equations is supplemented by the cohesion increment relationship given as:

$$\dot{c} = H_v\dot{\epsilon_v^p} - H_t\dot{T}, \tag{A.2}$$

where H_v and H_t are two material parameters, $\epsilon_v^p = \mathrm{tr}(\boldsymbol{\epsilon}^p)$ is the volumetric plastic strain.

As previously, the indices $n+1$ and n refer to the current and previous time steps, respectively. A discrete representation of system Eq. A.1a can be written as [25]:

$$\mathcal{F}\left(\boldsymbol{\sigma}''_{n+1}, c_{n+1}\right) = 0, \tag{A.3a}$$

$$-\boldsymbol{\epsilon}^p_{n+1} + \boldsymbol{\epsilon}^p_n + \Delta\lambda\frac{\partial \mathcal{F}}{\partial \boldsymbol{\sigma}''_{n+1}} = 0, \tag{A.3b}$$

$$\boldsymbol{\sigma}''_{n+1} - \boldsymbol{\sigma}''_n = \mathbb{C}\cdot\left(\boldsymbol{\epsilon}_{n+1} - \boldsymbol{\epsilon}_n - \boldsymbol{\epsilon}^p_{n+1} + \boldsymbol{\epsilon}^p_n\right) - \mathfrak{a}_{n+1}\left(T_{n+1} - T_n\right), \tag{A.3c}$$

$$c_{n+1} = c_n + H_v\left(\boldsymbol{\epsilon}^p_{v,n+1} - \boldsymbol{\epsilon}^p_{v,n}\right) - H_t\left(T_{n+1} - T_n\right), \tag{A.3d}$$

where $\Delta\lambda = \lambda_{n+1} - \lambda_n$. The values T_{n+1}, $\boldsymbol{\epsilon}_{n+1}$ are fixed during the return mapping step. System Eq. A.3d is nonlinear and can be solved [24] using Newton's method with respect to the primary unknowns $\left(\boldsymbol{\sigma}''_{n+1}, \Delta\lambda\right)$. However, this requires the calculation of the Hessian of the yield function, $\mathcal{F}$, which is a challenging procedure because of the need to compute the second derivatives of a complex function.

The solution $\left(\boldsymbol{\sigma}''_{n+1}, \Delta\lambda\right)$ of system (A.3d) implicitly depends on $\boldsymbol{\epsilon}$ and T. Consequently, the plastic strain $\boldsymbol{\epsilon}^p$ also depends on $\boldsymbol{\epsilon}$ and T. Thus, the incremental form of Eq. A.1c may be written as [46]:

$$\dot{\boldsymbol{\sigma}''} = \mathbb{C}^{ep}\cdot\dot{\boldsymbol{\epsilon}} - \mathbf{a}^{ep}\dot{T}. \tag{A.4}$$

To ensure a complete linearization of the global equations, the derivatives $\left(\frac{\partial \boldsymbol{\sigma}''}{\partial \boldsymbol{\epsilon}}, \frac{\partial \boldsymbol{\sigma}''}{\partial T}\right)$ must be derived, which is equivalent to the calculation of consistent elasto-plastic tensors $(\mathbb{C}^{\mathrm{ep}}, \mathbf{a}^{\mathrm{ep}})$. This is a critical aspect of the plasticity return-mapping algorithms [6, 13]. For this purpose, we employ an inverse-theorem approach implemented in AD-GPRS [61]. The system Eq. A.3d can be written in matrix notation as:

$$\mathbb{R}_7 = \mathbb{M}_{7\times 7}\cdot\mathbb{X}_7 = 0, \tag{A.5}$$

where $\mathbb{X}_7$ is the vector of unknowns (six components of $\boldsymbol{\sigma}''_{n+1}$ plus $\Delta\lambda$). After we obtain the solution $\mathbb{X}_7$, we compute the matrix of derivatives $\mathbb{J}_{7\times 7}$ as follows:

$$\mathbb{J}_{7\times 7} = \frac{\partial \mathbb{X}_7}{\partial \mathbb{Y}_7} = \left(\frac{\partial \mathbb{R}_7}{\partial \mathbb{X}_7}\right)^{-1}\cdot\frac{\partial \mathbb{R}_7}{\partial \mathbb{Y}_7}, \tag{A.6}$$

where $\mathbb{Y}_7 = (\boldsymbol{\epsilon}_{n+1}, T_{n+1})$. Then, the elasto-plastic tensors are simply the components of the matrix $\mathbb{J}_{7\times 7}$:

$$\left[\mathbb{C}^{\mathrm{ep}} \quad \mathbf{a}^{\mathrm{ep}}\right] = \mathbb{J}_{7\times 6} \tag{A.7}$$

Next, we consider the solution procedure for a given time interval (t_n, t_{n+1}). The state of the material is known at time step t_n, and we need to compute the stress $\boldsymbol{\sigma}_{n+1}$ and the tensors $\mathbf{a}_{n+1}$ and $\mathbb{C}_{n+1}$ at time step t_{n+1}. For this purpose,

we use an implicit integration algorithm. The fundamental idea relies on performing a predictor step in which the loading increment is elastic (plastic increment is zero). This allows us to estimate the current stress (trial solution) and evaluate the yield function. If the resulting yield function is less than zero, the trial solution is accepted and all internal state variables are updated assuming elastic deformation; otherwise, the trial state is incorrect and the material state should be plastic. In this case, we iteratively project stresses to the yield surface by solving Eq. A.3d. A high-level view of the basic steps is outlined in Algorithm 1.

Algorithm 1 Return-mapping algorithm

Require: $\boldsymbol{\epsilon}_{n+1}$, T_{n+1}
  Initialize: $l = 0$, $\boldsymbol{\epsilon}^p_{n+1,l} = \boldsymbol{\epsilon}^p_n$
  Update: $\mathbf{a} = \mathbf{a}(T_{n+1})$, $\mathbb{C} = \mathbb{C}(T_{n+1})$, and $c = c(T_{n+1})$
  Compute trial stress: $\boldsymbol{\sigma}''_{tr} = \mathbb{C} \cdot \left(\boldsymbol{\epsilon}_{n+1} - \boldsymbol{\epsilon}^p_{n+1,l}\right) - \mathbf{a} T_{n+1}$
  Evaluate yield function $\mathcal{F}\left(\boldsymbol{\sigma}''_{tr}, c\right)$
  if $\mathcal{F} \leq 0$ **then**
    Accept solution: $\boldsymbol{\sigma}''_{n+1} = \boldsymbol{\sigma}''_{tr}$, $\mathbb{C}^{ep}_{n+1} = \mathbb{C}$, $\mathbf{a}^{ep}_{n+1} = \mathbf{a}$
  else
    while $\mathcal{F} \neq 0$ **do**
      Solve Eq. A.3d for $\boldsymbol{\sigma}''_l$ and $\Delta\lambda_l$
      $l = l + 1$
    end while
    Calculate consistent moduli $\left(\mathbb{C}^{ep}_{n+1}, \mathbf{a}^{ep}_{n+1}\right)$ from Eqs. A.6 and A.7.
    Accept solution: $\boldsymbol{\sigma}''_{n+1} = \boldsymbol{\sigma}''_l$
    Update plastic strain $\boldsymbol{\epsilon}^p_{n+1}$ using Eq. A.3c
  end if
Ensure: $\boldsymbol{\sigma}''_{n+1}$, $\mathbb{C}^{ep}_{n+1}$, $\mathbf{a}^{ep}_{n+1}$

Appendix B: Solution strategies

In this section, we provide details of the implementation of the FI and SI schemes. For FI, the mass, energy, and momentum conservation equations are solved simultaneously, and the corresponding system of nonlinear equations is solved using Newton's method with a damped update. For the SI method, we partition the problem and solve each subproblem sequentially, iterating between the solutions. As previously, we define the fluid variables $R = (p, T, x)$ (pressure p, temperature T, and phase compositions x) and the mechanics variables $U = (\boldsymbol{u}, \boldsymbol{\epsilon}^p)$ (displacement u and plastic strain $\boldsymbol{\epsilon}^p$). We use the backward Euler time-integration scheme, where the simulation time step Δt is defined by $\Delta t = t_{n+1} - t_n$ and the indices $n+1$, n refer to the current and previous time steps, respectively. We always use the solution from the previous converged time step as the initial guess for the current time step (Algorithm 2[1]).

[1]The tolerance values ϵ_f, ϵ_m are used to ensure the convergence of each set of equations separately. The L_2 and L_∞ norms are used to control the tolerance values of "mechanics" and "flow/energy" equations, respectively.

Algorithm 2 Fully implicit solution strategy

Require: $R_n = (P_n, T_n, S_n, x_n)$, $U_n = \left(\boldsymbol{u}_n, \boldsymbol{\epsilon}_n, \boldsymbol{\epsilon}^e_n\right)$
  Set $R = R_n$ and $U = U_n$
  Set Newton's method iteration $i = 0$
  Calculate initial error norms for mass and energy $\|\mathcal{R}_f\|$, and for momentum balance equations $\|\mathcal{R}_m\|$
  while $\left(\|\mathcal{R}_f\| \geq \varepsilon_f, \quad \|\mathcal{R}_m\| \geq \varepsilon_m\right)$ **do**
    Solve mass, energy conservation equations and momentum balance equations for (R_{i+1}, U_{i+1}):
      Discretize Eq. 1, Eq. 3 and Eq. 7
      Calculate residual and Jacobian $\mathcal{R}(R_i, U_i)$, $\mathcal{J}(R_{i+1}, U_{i+1})$
      Solve system of linear equations
    Update all variables
      Update R_{i+1} and U_{i+1}
      Return mapping for plasticity
    Calculate error norms of $\mathcal{R} = (R_{i+1}, U_{i+1})$
    Set $i = i + 1$
  end while
Ensure: $R_{n+1} = R_i$, $U_{n+1} = U_i$
  Perform next time step t_{n+1}

Algorithm 3 Sequential-implicit solution strategy

Require: $R_n = (P_n, T_n, S_n, x_n)$, $U_n = \left(u_n, \boldsymbol{\epsilon}_n, \boldsymbol{\epsilon}^e_n\right)$
  Set sequential iteration $k = 0$
  Set $R_k = R_n$ and $U_k = U_n$
  Calculate initial error norms for mass and energy $\|\mathcal{R}_f\|$, and for momentum balance equations $\|\mathcal{R}_m\|$
  while $\left(\|\mathcal{R}_f\| \geq \varepsilon_f, \quad \|\mathcal{R}_m\| \geq \varepsilon_m\right)$ **do**
    repeat
      Solve mass and energy conservation equations for R_{k+1}:
        Update volumetric strain $\boldsymbol{\epsilon}_{v,k+1}$ (fixed-stress correction)
        Discretize Eq. 1, Eq. 3
        Calculate residual and Jacobian $\mathcal{R}_f(R_{k+1}, U_k)$, $\mathcal{J}_f(R_{k+1}, U_k)$
        Solve system of linear equations
      Update variables
        Update R_{k+1}
    until R_{k+1} converges
    Calculate error norm of $\mathcal{R}_m(R_{k+1}, U_k)$

    repeat
      Solve momentum balance equations for U_{k+1}
        Use fixed R_{k+1}
        Discretize Eq. 7
        Calculate residual and Jacobian $\mathcal{R}_m(R_{k+1}, U_{k+1})$, $\mathcal{J}_m(R_{k+1}, U_{k+1})$
        Solve system of linear equations
      Update variables
        Update U_{k+1}
        Return mapping algorithm for plasticity
    until U_{k+1} converges
    Calculate error norm of $\mathcal{R}_f(R_{k+1}, U_{k+1})$,
    Set $k = k + 1$
  end while
Ensure: $R_{n+1} = R_k$, $U_{n+1} = U_k$
  Perform next time step t_{n+1}

References

1. Aboustit, B., Advani, S., Lee, J.: Variational principles and finite element simulations for thermo-elastic consolidation. Int. J.

Numer. Anal. Methods Geomech. **9**, 49–69 (1985). https://doi.org/10.1002/nag.1610090105
2. AD-GPRS: Automatic differentiation general purpose research simulator. https://supri-b.stanford.edu/research-areas/ad-gprs (2017)
3. Armero, F., Simo, J.: A new unconditionally stable fractional step method for non-linear coupled thermomechanical problems. Int. J. Numer. Methods Eng. **35**, 737–766 (1992). https://doi.org/10.1002/nme.1620350408
4. Aziz, K., Settari, A.: Petroleum reservoir simulation. Applied Science Publishers (1979)
5. Bevillon, D., Masson, R.: Stability and convergence analysis of partially coupled schemes for geomechanical reservoir simulations. In: The European Conference on the Mathematics of Oil Recovery. Baveno, Italy (2000)
6. Borja, I.: Plasticity: modeling and computation. Springer, Berlin (2013)
7. Butler, R.: New approach to the modelling of steam-assisted gravity drainage. J. Can. Pet. Technol. **24**, 42–51 (1985). https://doi.org/10.2118/85-03-01
8. Cao, H., Tchelepi, H.A., Wallis, J.R., Yardumian, H.E.: Parallel scalable unstructured CPR-type linear solver for reservoir simulation. In: SPE Annual Technical Conference and Exhibition. Society of Petroleum Engineers (2005)
9. Castelletto, N., White, J.A., Tchelepi, H.A.: Accuracy and convergence properties of the fixed-stress iterative solution of two-way coupled poromechanics. Int. J. Numer. Anal. Methods Geomech. **39**, 1593–1618 (2015). https://doi.org/10.1002/nag.2400
10. Christie, M., Blunt, M.: Tenth SPE comparative solution project: a comparison of upscaling techniques. In: SPE Reservoir Simulation Symposium. Society of Petroleum Engineers (2001)
11. Coats, K.H.: An equation of state compositional model. Society of Petroleum Engineers (1980). https://doi.org/10.2118/8284-PA
12. Coussy, O.: Poromechanics. Wiley, New York (2004)
13. Crisfield, M.: Non-linear finite element analysis of solids and structures. Wiley, New York (1996)
14. David, C., Wong, T.-F., Zhu, W., Zhang, J.: Laboratory measurement of compaction-induced permeability change in porous rocks: implications for the generation and maintenance of pore pressure excess in the crust. Pure Appl. Geophys. **143**, 425–456 (1994). https://doi.org/10.1007/BF00874337
15. Dean, R., Gai, X., Stone, C., Minkoff, S.: A comparison of techniques for coupling porous flow and geomechanics. Soc. Petrol. Eng. **11**, 132–140 (2006). https://doi.org/10.2118/79709-PA
16. Drucker, D., Prager, W.: Soil mechanics and plastic analysis or limit design. Q. Appl. Math. **10**, 157–165 (1952)
17. Ehlers, W., Ellsiepen, P.: Pandas: Ein fe-system zur simulation von sonderproblemen der bodenmechanik. Finite Elemente in der Baupraxis: Modellierung, Berechnung und Konstruktion. Beiträge zur Tagung FEM **98**, 431–400 (1998)
18. Fedorenko, R.: A relaxation method for solving elliptic difference equations. USSR Comput. Math. Math. Phys. **1**, 1092–1096 (1962)
19. Flemisch, B., Darcis, M., Erbertseder, K., Faigle, B., Lauser, A., Mosthaf, K., Müthing, S., Nuske, P., Tatomir, A., Wolff, M., Helmig, R.: DuMux: DUNE for multi-{phase,component,scale,physics,...} flow and transport in porous media. Adv. Water Resour. **34**, 1102–1112 (2011). https://doi.org/10.1016/j.advwatres.2011.03.007
20. Gai, X.: A coupled geomechanics and reservoir flow model on parallel computers. Ph.D. thesis University of Texas at Austin (2004)
21. Garipov, T.T., Voskov, D., Tchelepi, H.A.: Rigorous coupling of geomechanics and thermal-compositional flow for SAGD and ES-SAGD operations. In: SPE Canada Heavy Oil Technical Conference. Calgary, Canada (201 5). https://doi.org/10.2118/174508-MS
22. Garipov, T.T., White, J., Lapene, A., Tchelepi, H.A.: Thermo-hydro-mechanical model for source rock thermal maturation. In: 50th US Rock Mechanics Geomechanics Symposium 2016. Houston, USA (2016)
23. Hu, L., Winterfeld, P.H., Fakcharoenphol, P., Wu, Y.-S.: A novel fully-coupled flow and geomechanics model in enhanced geothermal reservoirs. J. Pet. Sci. Eng. **107**, 1–11 (2013). https://doi.org/10.1016/j.petrol.2013.04.005
24. Huang, J., Griffiths, D.: Return mapping algorithms and stress predictors for failure analysis in geomechanics. J. Eng. Mech. **135**, 276–284 (2009). https://doi.org/10.1061/(ASCE)0733-9399(2009)135:4(276)
25. Hughes, T.: The finite element method: linear static and dynamic finite element analysis. Courier Dover Publications (2012)
26. Jha, B., Juanes, R.: A locally conservative finite element framework for the simulation of coupled flow and reservoir geomechanics. Acta Geotech. **2**, 139–153 (2007). https://doi.org/10.1007/s11440-007-0033-0
27. Keilegavlen, E., Nordbotten, J.M.: Finite volume methods for elasticity with weak symmetry. International Journal for Numerical Methods in Engineering (2017)
28. Kim, J.: Sequential methods for coupled geomechanics and multiphase flow. Ph.D. thesis Stanford University (2010)
29. Kim, J.: Unconditionally stable sequential schemes for thermoporomechanics: undrained-adiabatic and extended fixed-stress splits. In: SPE Reservoir Simulation Symposium. Houston, USA (2015). https://doi.org/10.2118/173294-MS
30. Kim, J., Tchelepi, H., Juanes, R.: Stability and convergence of sequential methods for coupled flow and geomechanics: fixed-stress and fixed-strain splits. Comput. Methods Appl. Mech. Eng. **200**, 1591–1606 (2011). https://doi.org/10.1016/j.cma.2010.12.022
31. Kim, J., Tchelepi, H.A., Juanes, R.: Rigorous coupling of geomechanics and multiphase flow with strong capillarity. SPE J **18**, 1–123 (2013)
32. Klevtsov, S., Castelletto, N., White, J., Tchelepi, H.: Block-preconditioned Krylov methods for coupled multiphase reservoir flow and geomechanics. In: ECMOR XIV-15th European Conference on the Mathematics of Oil Recovery (2016)
33. Kolditz, O., Bauer, S., Bilke, L., Bottcher, N., Delfs, J., Fischer, T., Gorke, U., Kalbacher, T., Kosakowski, G., Mcdermott, C., Park, C., Radu, F., Rink, K., Shao, H., Shao, H., Sun, F., Sun, Y., Singh, A., Taron, J., Walther, M., Wang, W., Watanabe, N., Wu, Y., Xie, M., Xu, W., Zehner, B.: Opengeosys: an open-source initiative for numerical simulation of thermo-hydro-mechanical/chemical (THM/C) processes in porous media. Environ. Earth Sci. **67**, 589–599 (2012). https://doi.org/10.1007/s12665-012-1546-x
34. Lewis, R.W., Schrefler, B.A.: The finite element method in the static and dynamic deformation and consolidation of porous media. Wiley, New York (1998)
35. Li, P., Chalaturnyk, R.: Gas-over-bitumen geometry and its SAGD performance analysis with coupled reservoir geomechanical simulation. J. Can. Pet. Technol. **46**, 42–49 (2007). https://doi.org/10.2118/07-01-05
36. Li, P., Chalaturnyk, R., et al.: History match of the UTF phase A project with coupled reservoir geomechanical simulation. In: Canadian International Petroleum Conference. Petroleum Society of Canada (2005)
37. Lie, K.-A.: An introduction to reservoir simulation using MATLAB: user guide for the Matlab Reservoir Simulation Toolbox (MRST). SINTEF ICT (2014)
38. Mainguy, M., Longuemare, P.: Coupling fluid flow and rock mechanics: formulations of the partial coupling between reservoir and geomechanical simulators. Oil Gas Sci. Technol. **57**, 355–367 (2002)

39. Mandel, J.: Consolidation des sols (étude mathématique). Geotechnique **3**, 287–299 (1953)
40. Markert, B., Heider, Y., Ehlers, W.: Comparison of monolithic and splitting solution schemes for dynamic porous media problems. Int. J. Numer. Methods Eng. **82**, 1341–1383 (2010). https://doi.org/10.1002/nme.2789
41. Mikelic, A., Wheeler, M.: Convergence of iterative coupling for coupled flow and geomechanics. Comput. Geosci. **17**, 455–461 (2013). https://doi.org/10.1007/s10596-012-9318-y
42. Minkoff, S., Stone, C., Bryant, S., Peszynska, M., Wheeler, M.: Coupled fluid flow and geomechanical deformation modeling. J. Pet. Sci. Eng. **38**, 37–56 (2003a). https://doi.org/10.1016/S0920-4105(03)00021-4
43. Minkoff, S.E., Stone, C., Bryant, S., Peszynska, M., Wheeler, M.F.: Coupled fluid flow and geomechanical deformation modeling. J. Pet. Sci. Eng. **38**, 37–56 (2003b). https://doi.org/10.1016/S0920-4105(03)00021-4
44. Nikolaevskij, V.N.: Mechanics of porous and fractured media volume 8. World Scientific (1990)
45. Noorishad, J., Tsang, C.F., Witherspoon, P.A.: Coupled thermal-hydraulic-mechanical phenomena in saturated fractured porous rocks: numerical approach. J. Geophys. Res. Solid Earth **89**, 10365–10373 (1984). https://doi.org/10.1029/JB089iB12p10365
46. Ottosen, N., Ristinmaa, M.: The Mechanics of Constitutive Modeling. Elsevier, Amsterdam (2005)
47. Park, K.: Stabilization of partitioned solution procedure for pore fluid-soil interaction analysis. Int. J. Numer. Methods Eng. **19**, 1669–1673 (1983). https://doi.org/10.1002/ nme.1620191106
48. Peneloux, A., Rauzy, E., Freze, R.: A consistent correction for Redlich-Kwong-Soave volumes. Fluid Phase Equilib. **8**, 7–23 (1982). https://doi.org/10.1016/0378-3812(82)80002-2
49. Prevost, J.H.: Partitioned solution procedure for simultaneous integration of coupled-field problems. Commun. Numer. Methods Eng. **13**, 239–247 (1997). https://doi.org/10.1002/(SICI)1099-0887(199704)13:43.0.CO;2-2
50. Rahmati, E., Nouri, A., Fattahpour, V., et al.: Caprock integrity analysis during a sagd operation using an anisotropic elasto-plastic model. In: SPE Heavy Oil Conference-Canada. Society of Petroleum Engineers (2014)
51. Rin, R.: Implicit Coupling Framework for Multi-Physics Reservoir Simulation. Ph.D. thesis Stanford University (2017)
52. Rin, R., Tomin, P., Garipov, T., Voskov, D., Tchelepi, H.: General implicit coupling framework for multi-physics problems. In: SPE-182714-MS, SPE Reservoir Simulation Conference. Montgomery, USA (2017)
53. Rutqvist, J.: Status of the tough-flac simulator and recent applications related to coupled fluid flow and crustal deformations. Comput. Geosci. **37**, 739–750 (2011). https://doi.org/10.1016/j.cageo.2010.08.006.2009 Transport of Unsaturated Groundwater and Heat Symposium
54. Samier, P., Onaisi, A., de Gennaro, S.: A practical iterative scheme for coupling geomechanics with reservoir simulation. SPE Reserv. Eval. Eng. **11**, 892–901 (2008). https://doi.org/10.2118/107077-PA
55. Settari, A., Walters, D.: Advances in coupled geomechanical and reservoir modeling with applications to reservoir compaction. Soc. Petrol. Eng. **6**, 14–17 (2001). https://doi.org/10.2118/74142-PA
56. Simo, J.C., Hughes, T.J.: Computational Inelasticity volume 7. Springer Science Business Media (2006)
57. Stüben, K.: Algebraic multigrid (AMG): experiences and comparisons. Appl. Math. Comput. **13**, 419–451 (1983). https://doi.org/10.1016/0096-3003(83)90023-1
58. Thomas, L., Chin, L., Pierson, R., Sylte, J.: Coupled geomechanics and reservoir simulation. Soc. Petrol. Eng. **8**, 350–358 (2003). https://doi.org/10.2118/87339-PA
59. Tran, D., Settari, A., Nghiem, L.: New iterative coupling between a reservoir simulator and a geomechanics module. Soc. Petrol. Eng. **9**, 362–369 (2004). https://doi.org/10.2118/88989-PA
60. Voskov, D., Zaydullin, R., Lucia, A.: Heavy oil recovery efficiency using SAGD, SAGD with propane co-injection and STRIP-SAGD. Comput. Chem. Eng. **88**, 115–125 (2016). https://doi.org/10.1016/j.compchemeng.2016.02.010
61. Voskov, D.V., Tchelepi, H.A.: Comparison of nonlinear formulations for two-phase multi-component EoS based simulation. J. Pet. Sci. Eng. **82–83**, 101–111 (2012). https://doi.org/10.1016/j.petrol.2011.10.012
62. Wallis, J.R.: Incomplete gaussian elimination as a preconditioning for generalized conjugate gradient acceleration. In: 7th SPE Reservoir Simulation Symposium. San Francisco, USA (1983). https://doi.org/https://doi.org/10.2118/12265-MS
63. Wheeler, M.F., Gai, X.: Iteratively coupled mixed and Galerkin finite element methods for poro-elasticity. Num Methods Partial Differential Equations **23**, 785–797 (2007). https://doi.org/10.1002/num.20258
64. White, J.A., Castelletto, N., Tchelepi, H.A.: Block-partitioned solvers for coupled poromechanics: a unified framework. Comput. Methods Appl. Mech. Eng. **303**, 55–74 (2016). https://doi.org/10.1016/j.cma.2016.01.008
65. White, M., Oostrom, M.: Stomp: subsurface transport over multiple phases. version 4.0, user's guide. Richland: Pacific Northwest National Laboratory (2006)
66. Yang, D., Moridis, G.J., Blasingame, T.A.: A fully coupled multiphase flow and geomechanics solver for highly heterogeneous porous media. J. Comput. Appl. Math. **270**, 417–432 (2014). https://doi.org/10.1016/j.cam.2013.12.029
67. Younis, R.M.: Modern advances in software and solution algorithms for reservoir simulation. Ph.D. thesis Stanford University (2011)
68. Zaydullin, R., Voskov, D., Tchelepi, H.: Comparison of eos-based and k-values-based methods for three-phase thermal simulation. Transport in Porous Media, (pp. 1–24) (2016a). https://doi.org/10.1007/s11242-016-0795-7
69. Zaydullin, R., Voskov, D., Tchelepi, H.: Phase-state identification bypass method for three-phase thermal compositional simulation. Comput. Geosci. **20**, 461–474 (2016b). https://doi.org/10.1007/s10596-015-9510-y
70. Zhou, Y., Jiang, Y., Tchelepi, H.: A scalable multistage linear solver for reservoir models with multisegment wells. Comput. Geosci. **17**, 197–216 (2013a). https://doi.org/10.1007/s10596-012-9324-0
71. Zhou, Y., Jiang, Y., Tchelepi, H.A.: A scalable multistage linear solver for reservoir models with multisegment wells. Comput. Geosci. **17**, 197–216 (2013b)
72. Zienkiewicz, O., Paul, D., Chan, A.: Unconditionally stable staggered solution procedure for soil-pore fluid interaction problems. Int. J. Numer. Methods Eng. **26**, 1039–1055 (1988). https://doi.org/10.1002/nme.1620260504
73. Zienkiewicz, O., Taylor, R.: The finite element method for solid and structural mechanics. Elsevier, Amsterdam (2005)